

# Polaronic Competition Triggers the H<sub>2</sub>O<sub>2</sub> Evolution on Perovskite Oxides during Water Oxidation

Mohsen Sotoudeh\* and Axel Groß\*

Cite This: *ACS Catal.* 2025, 15, 11544–11553

Read Online

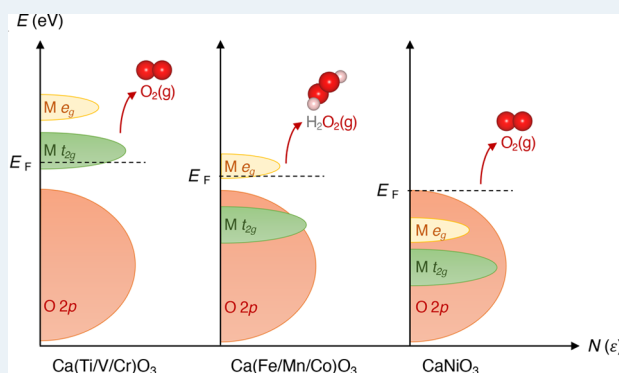
ACCESS |

Metrics &amp; More

Article Recommendations

**ABSTRACT:** Perovskite oxides, particularly calcium-based perovskites (CaMO<sub>3</sub>), are promising catalysts for the oxygen evolution reaction (OER) due to their high efficiency and economic feasibility. However, a comprehensive mechanistic understanding that elucidates the relationship between catalytic selectivity and mechanistic pathways has yet to be achieved. In this study, we employ density functional theory (DFT) to investigate the mechanism of the OER in a series of Ca-based perovskites. Our findings indicate that early transition metals in CaMO<sub>3</sub> favor a conventional OER pathway, characterized by a four-step concerted proton–electron transfer process leading to O<sub>2</sub> formation from H<sub>2</sub>O. In contrast, perovskites containing Mn, Fe, and Co exhibit two proton–electron transfer steps, favoring the selective formation of hydrogen peroxide (H<sub>2</sub>O<sub>2</sub>) over O<sub>2</sub>. This shift in selectivity is attributed to polaronic effects, which strengthen the metal–oxo bonding, enabling a transition from a conventional OER to H<sub>2</sub>O<sub>2</sub> evolution. Furthermore, we reveal that the thermodynamic stability of these perovskites in aqueous environments is significantly influenced by pH, where acidic conditions destabilize the perovskite structure. These insights suggest that modulating polaronic effects and maintaining high pH environments are key to optimizing both the stability and catalytic activity of perovskite oxides in OER applications.

**KEYWORDS:** perovskite oxides, oxygen evolution reaction, hydrogen peroxide, density functional theory, catalytic selectivity, polaronic effects, aqueous stability



## INTRODUCTION

The oxygen evolution reaction (OER) on metal oxide surfaces offers a promising avenue for the development of materials for clean energy and environmental applications. This O–O dimerization reaction, which is governed by complex electron transfer processes, is key to the performance of technological devices such as water-splitting devices,<sup>1,2</sup> fuel cells,<sup>3</sup> rechargeable metal–air batteries<sup>4,5</sup> and the storage of energy in lithium-ion battery materials.<sup>6,7</sup> The current understanding of the OER mechanism suggests that four sequential concerted proton–electron transfer steps ( $2\text{H}_2\text{O} \rightarrow \text{O}_2 + 4\text{H}^+ + 4\text{e}^-$ ) yield molecular oxygen from water,<sup>8,9</sup> resulting in a pH-independent activity on the reversible hydrogen electrode (RHE) scale.<sup>10</sup> In this mechanism, high OER activities can be achieved by tuning the binding strength of reaction intermediates on oxide surfaces,<sup>11</sup> correlating with electronic structure parameters such as the  $e_g$  occupancy of surface transition-metal ions.<sup>12</sup> However, recent observations have called into question this established mechanism, proposing instead the involvement of lattice oxygen redox chemistry,<sup>13–15</sup> nonconcerted proton–electron transfers,<sup>10</sup> and pH-dependent OER activity.<sup>16–18</sup>

An alternative product in the water oxidation reaction is hydrogen peroxide (H<sub>2</sub>O<sub>2</sub>), formed via a two-electron transfer process ( $2\text{H}_2\text{O} \rightarrow \text{H}_2\text{O}_2 + 2\text{H}^+ + 2\text{e}^-$ ), which competes with the four-electron OER pathway.<sup>19,20</sup> The selective production of H<sub>2</sub>O<sub>2</sub> is of considerable interest due to its broad industrial applications, notably in electrochemical systems,<sup>21</sup> fuel cells,<sup>22</sup> and rechargeable metal–hydrogen peroxide batteries.<sup>23</sup> Catalytic systems that selectively favor H<sub>2</sub>O<sub>2</sub> production over O<sub>2</sub> evolution require the controlled stabilization of key reaction intermediates, such as metal hydroxide OH\*, to promote the desired two-electron transfer process.<sup>19,24</sup> However, excessive stabilization of this intermediate can inadvertently stabilize the solvated hydroxyl radical  $\cdot\text{OH}$  ( $\text{H}_2\text{O} \rightarrow \cdot\text{OH}(\text{aq}) + \text{H}^+ + \text{e}^-$ ), thereby detracting from efficient H<sub>2</sub>O<sub>2</sub> formation.<sup>24</sup> Consequently, a detailed understanding of the mechanistic

Received: March 24, 2025

Revised: June 4, 2025

Accepted: June 9, 2025

Published: June 20, 2025



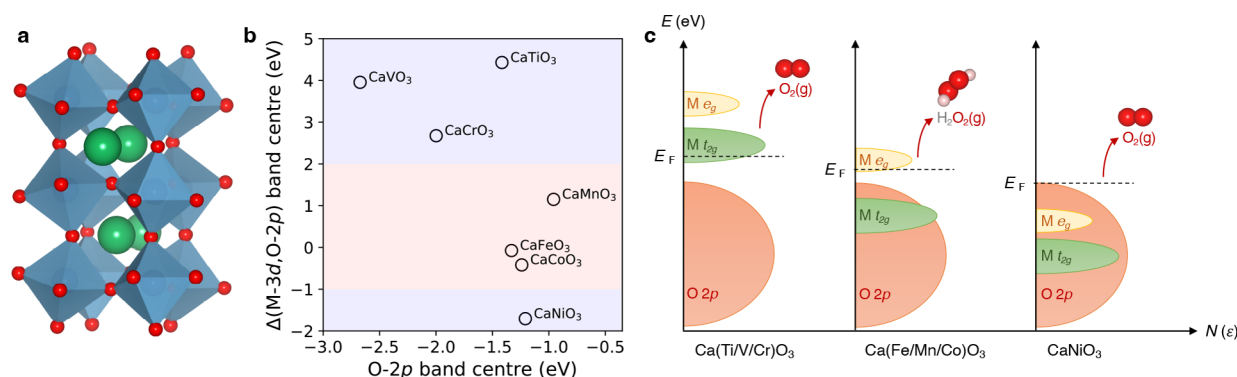


**Figure 1.** Structural and electronic properties of  $CaMO_3$  perovskites. (a) Crystal structure of perovskite oxides with octahedral tilting and orthorhombic  $Pnma$  (#62) space group. The red spheres denote oxygen anions, and the green spheres depict calcium cations. The blue polyhedra represent the transition metals in the octahedral sites. (b) Relative band centers between O 2p and transition metals 3d versus the O 2p band center with respect to the Fermi level for  $CaMO_3$  perovskites. The band centers of perovskite oxides are obtained from DFT calculations. (c) Schematic representations of density of states (DOS) diagrams in a projective view for  $CaMO_3$ . The graphs show the schematic projected DOS for O 2p (red), M  $t_{2g}$  (green), and M  $e_g$  (yellow). The dashed line is the Fermi level ( $E_F$ ).

distinctions between the two- and four-electron transfer pathways is essential for the rational design of advanced electrodes and electrocatalysts. Such insights will enable more precise control over product selectivity, efficiency, and energy demands in both renewable energy applications and selective chemical synthesis systems.

This study aims to elucidate the fundamental principles governing the competing four-electron  $O_2$  evolution and two-electron  $H_2O_2$  evolution pathways, addressing critical challenges in electrocatalysis. We explore a series of perovskites,  $CaMO_3$ , by using periodic density functional theory (DFT) and thermodynamic stability analysis. We have particularly chosen this type of material because of the tunable constitutions and structures with a strong octahedral tilting<sup>25</sup> that exhibit superb OER reactivity comparable to that of precious metal oxides.<sup>12</sup> Our simulations reveal that early transition metals preferentially stabilize metal-oxo complexes ( $O^*$ ), supporting four concerted proton–electron transfer steps and favoring the evolution of the  $O_2$  from water. In contrast, transition metals such as Mn, Fe, and Co show selectivity toward  $H_2O_2$  production. In light of these findings, we discuss the potential for  $H_2O_2$  production correlating with the presence of polarons in perovskite compounds and the stabilization of key reaction intermediates,  $O^*$ . Furthermore, Pourbaix diagrams will be presented to demonstrate the pH-dependent thermodynamic stability of perovskites in aqueous environments.

## RESULTS AND DISCUSSION

### Structural Properties and the Reaction Mechanism.

Calcium perovskite oxides with the general formula of  $CaMO_3$  crystallize in the  $Pnma$  space group, where each oxygen atom is shared between two transition metal (M) ions, each coordinated octahedrally (Figure 1a). This arrangement induces a crystal field effect, resulting in the splitting of the transition metal 3d orbitals into three lower-energy  $t_{2g}$  orbitals and two higher-energy  $e_g$  orbitals.<sup>26,27</sup> The  $e_g$  orbitals overlap with the oxygen p orbitals to form  $\sigma$  bonds, while the  $t_{2g}$  orbitals engage in  $\pi$  bonding interactions. A three-dimensional integration of these states produces a density of states (DOS) diagram, providing a detailed representation of the electronic density associated with each orbital state.

Understanding the role of metal–oxygen covalency in the evolution of the compound  $O_2$  and its competitor  $H_2O_2$  is

essential. Our DFT studies reveal that substituting transition metals at the M-site in the perovskite structure ( $CaMO_3$ ) shifts the Fermi level across the metal d-band, which in turn alters the position of the d-band center relative to the O 2p-band center (Figure 1b). As the d-band, from  $CaTiO_3$  to  $CaNiO_3$ , moves down in energy upon higher occupancy and approaches the O 2p states, the antibonding states below the Fermi level show increased oxygen character, indicating enhanced covalency in the metal–oxygen bond. When the O 2p states at the Fermi level are positioned above the d orbital and exceed the redox potential of the  $O_2/H_2O$  pair, as reported by Grimaud et al.,<sup>14</sup> the oxidation of lattice oxygen in perovskites becomes thermodynamically favorable.

Our calculations demonstrate that perovskites exhibiting the  $3d^0$  to  $3d^2$  configurations during the OER are associated with a weaker  $\pi$ -bond and linked to the conventional OER mechanism involving four-step proton–electron transfer processes (Figure 1c). Late transition metal perovskites also generate  $O_2$  via an adsorbate evolution mechanism, as well as activating lattice oxygen. Experimental studies have confirmed that the oxygen evolved on certain Co-based oxides can originate from the lattice itself,<sup>13–15</sup> overcoming limitations of the adsorbate evolution mechanism imposed by scaling relations. In contrast, the  $3d^3$  to  $3d^5$  configurations involve the redox of the cations with  $\sigma$  character, deviating from the conventional OER mechanism and leading to the evolution of hydrogen peroxide ( $H_2O_2$ ) (Figure 1c). This suggests that increased metal–oxygen covalency correlates with increasing  $H_2O_2$  evolution activity. According to the Pauli principle, the participation of the  $e_g$  orbitals affects the local structure around the transition metal cations, giving rise to the formation of polarons.<sup>26,28,29</sup>

Polarons correspond to composite quasi-particles that are formed due to the local polarization of a crystal lattice caused by the presence of charged particles. They stand apart from defects,<sup>30</sup> showcasing superior mobility characteristics in crystal structures.<sup>29</sup> In perovskite structures, Jahn–Teller type distortions localized around the transition metal sites and the formation of so-called Zener polarons involving ferromagnetic coupling between pairs of transition metal ions have been observed.<sup>31</sup> These quasi-particles are commonly formed in a variety of materials, including polar semiconductors, ionic crystals, organic semiconductors, and hybrid perovskites.<sup>32</sup> Examples of such materials include  $TiO_2$ ,<sup>33,34</sup>  $SrTiO_3$ ,<sup>35</sup>

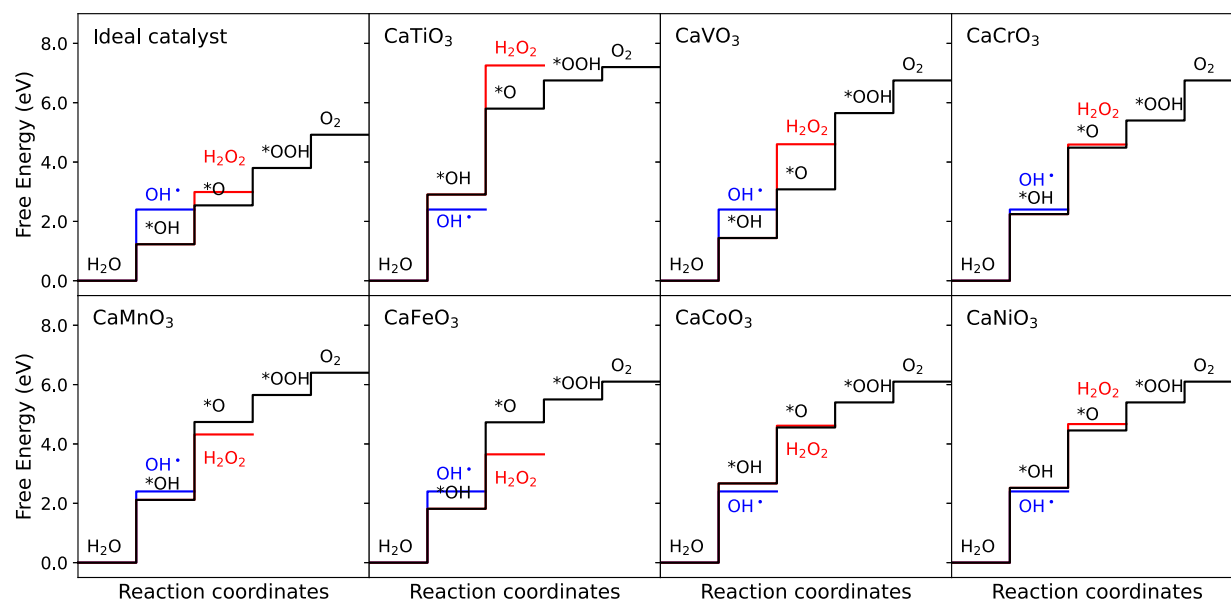


**Figure 2.** Theoretical OER free energy diagrams for various  $\text{CaMO}_3$  perovskites at zero potential. The black line shows the conventional proton–electron transfer on the surface while the red line represents  $\text{H}_2\text{O}_2$  evolution through the hemibonded structure. The blue line represents hydroxyl radicals with  $\Delta G_{\text{OH(aq)}} = 2.4$  eV. The ideal catalyst would exhibit a free energy profile where all intermediates are thermodynamically balanced, minimizing overpotentials relative to the thermodynamic potential of 1.23 eV.

$\text{Fe}_2\text{O}_3$ ,<sup>36</sup> and  $\text{BiVO}_4$ .<sup>37</sup> The introduction of polarons has been demonstrated to exert a significant influence on a range of properties, including light absorption, charge separation and transfer, surface reactivity, molecular adsorption/desorption, and local electronic characteristics.<sup>38–40</sup> Nevertheless, their relationship to the reaction path in the OER has only recently been the subject of investigation, resulting in reducing the overpotential of the reaction-determining step<sup>41</sup> and affecting the band alignment at the solid/liquid interface that competes with the evolution of the water-splitting reaction.<sup>42</sup>

**Kinetics of the Water Oxidation.** The electron/hole transfer during the electrochemical process can lead to the conventional proton–electron transfer mechanism, the formation of oxonium-like complexes such as  $\text{H}_3\text{O}^+\cdot\text{OH}$ , or water-like complexes like  $[\text{H}_2\text{O}\cdot\text{H}_2\text{O}]^+$ , resulting in a hemibonded structure.<sup>43–45</sup> In the latter case, the hole localizes between two oxygen ions, and the doubly oxidized water dimer forms a true O–O bond (bond distance  $\sim 1.5$  Å), which subsequently leads to the formation of hydrogen peroxide ( $\text{H}_2\text{O}_2$ ).<sup>43</sup> These findings based on the simplified model of the water dimer cation provide a foundation for understanding the potential observation of hemibonded structures in electrochemical water oxidation. We have recently demonstrated that a substantial energy barrier hinders transformation into the proton-transferred structure.<sup>43</sup> This implies that hemibonded structures may have a lifespan sufficient to allow them to undergo double oxidation.

In order to evaluate selectivity trends for two corresponding reactions, namely, the  $\text{H}_2\text{O}_2$  and  $\text{O}_2$  production, free energy diagrams are constructed for an ideal catalyst along with all considered  $\text{CaMO}_3$  catalysts (Figure 2). The diagrams have been developed on the basis of the adsorption free energies of the relevant intermediates involved in two-electron and four-electron water oxidation reactions, specifically  $\text{OH}^*$ ,  $\text{O}^*$ , and  $\text{OOH}^*$ . The computational hydrogen electrode (CHE)<sup>8</sup> model is utilized, which is based on the fact that the chemical potential of a proton–electron pair is equivalent to that of gas-phase  $\text{H}_2$  at an electrode potential of  $U = 0.0$  V relative to the reversible

hydrogen electrode (RHE).<sup>10,46</sup> The impact of the electrode potential on the free energy of the intermediates is incorporated by making an adjustment to the electron energy with a value of  $-eU$ . Here,  $e$  represents the elementary charge, while  $U$  denotes the electrode potential on the RHE scale.

We initiated our investigation by examining the free energy diagram of  $\text{CaTiO}_3$ . The most prominent thermodynamic energy barrier identified is associated with the initial oxidation step ( $\Delta G_{\text{OH}^*} = 2.9$  eV), which leads to the formation of adsorbed hydroxyl groups ( $\text{OH}^*$ ). Notably, the energy required for this step is larger than that of solvated hydroxyl radicals ( $\Delta G_{\text{OH(aq)}} = 2.4$  eV<sup>24</sup>), indicating that once  $\text{OH}^*$  is generated, it is thermodynamically favorable for it to desorb as a solvated hydroxyl radical rather than recombine at the surface to produce a metal hydroxide group. This suggests a strong tendency for  $\text{CaTiO}_3$  to generate hydroxyl radicals, aligning with experimental findings from UV-illuminated  $\text{CaTiO}_3$ , which demonstrate the production of hydroxyl radicals with the energy of holes during UV exposure estimated at around 2.5 V.<sup>47</sup> Furthermore, the free energy of  $\text{H}_2\text{O}_2$  is significantly higher than that of  $\text{O}^*$ , indicating that the metal-oxo complex ( $\text{O}^*$ ) could serve as a potential secondary oxidation product.

The preceding analysis indicates that a criterion for the generation of hydroxyl radicals is that the free energy of the hydroxyl species ( $\text{OH}^*$ ) on the catalyst surface must be greater than that of aqueous hydroxyl radicals ( $\text{OH(aq)}$ ), which has a free energy of approximately 2.4 eV.<sup>24</sup> This greater free energy is required for the generation of hydroxyl radicals, as the free energy of the hydroxyl species on the catalyst surface must be endergonic relative to that of water. This establishes an upper threshold for the free energy of  $\text{OH}^*$  on the surface during the formation of an oxygen molecule or hydrogen peroxide. Therefore, in order to avoid the one-electron oxidation reaction ( $\text{H}_2\text{O} \rightarrow \cdot\text{OH(aq)} + \text{H}^+ + \text{e}^-$ ) and facilitate the two/four-electron oxidation pathways, it is necessary that  $\Delta G_{\text{OH}^*}$  should be less than or equal to 2.4 eV.



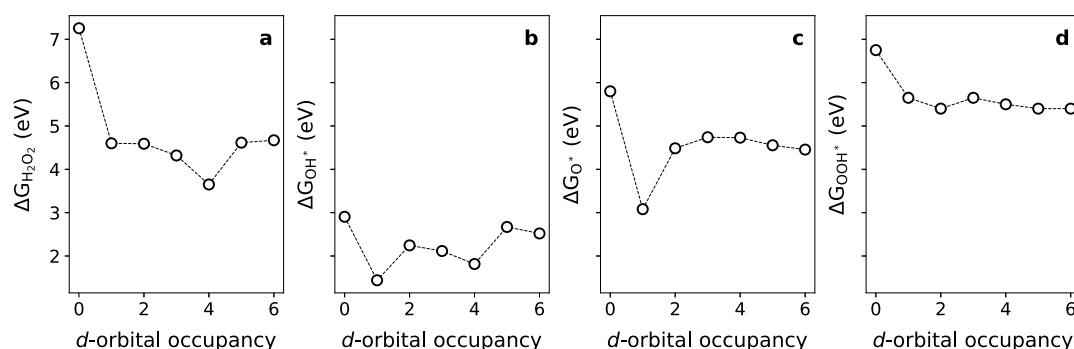


**Figure 3.** Activity trends toward the OER. The free energy of (a),  $\text{H}_2\text{O}_2$ , (b),  $\text{OH}^*$ , (c),  $\text{O}^*$ , and (d)  $\text{OOH}^*$  on the  $\text{CaMO}_3$  perovskites as a function of the  $d$ -orbital occupancy. The considered  $d$ -orbital occupancy corresponds to the sequence Ti, V, Cr, Mn, Fe, Co, and Ni.

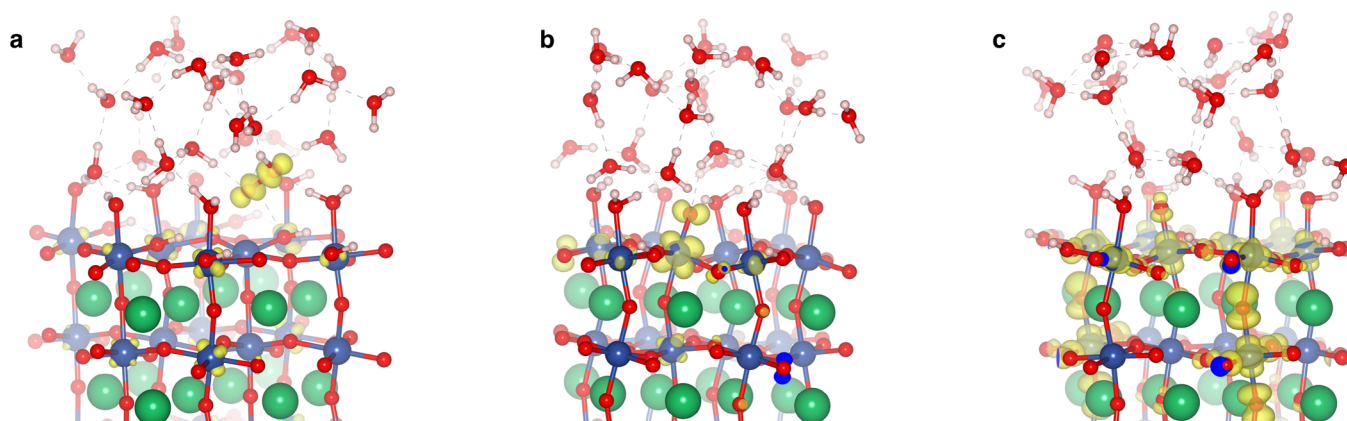


**Figure 4.** Orbital representation of the states caused by the second deprotonation. (a) Representation of  $\sigma$ -bond caused by hole localization between two oxygen molecules. (b)  $\pi$ -bond formation between the transition metal  $3d-t_{2g}$  and adsorbed oxygen  $2p$ -orbital. (c)  $\sigma$ -bond formation between the transition metal  $3d-e_g$  and adsorbed oxygen  $2p$ -orbital as a part of the polaronic states.

We will now discuss the consequences of the calculated free energy diagram in Figure 2 for the remaining Ca perovskites with respect to their suitability as OER catalysts. The calculated free energy diagram demonstrates that  $\text{CaVO}_3$  might act as an effective catalyst for oxygen evolution. The adsorption of hydroxyl species ( $\Delta G_{\text{OH}^*} = 1.4$  eV) on  $\text{CaVO}_3$  is well documented, with its free energy being significantly lower than that associated with the formation of hydroxyl radicals. Furthermore, the free energy associated with the adsorption of oxygen species ( $\Delta G_{\text{O}^*} = 3.0$  eV) is markedly lower than that for hydrogen peroxide, indicating that the  $\text{CaVO}_3$  surface provides a substantial driving force for the complete four-electron oxidation process.

The free energy profile for  $\text{CaCrO}_3$  indicates that the initial oxidation step, which leads to the formation of adsorbed hydroxyl species ( $\Delta G_{\text{OH}^*} = 2.2$  eV), requires less energy than that associated with the hydroxyl radical formation. Consequently, from a thermodynamic perspective, adsorbed hydroxyl species are stabilized on the surface, favoring the formation of a metal hydroxide group. In the subsequent oxidation step, the system shows energetic feasibility for pathways leading either to a metal-oxo species or to the generation of hydrogen peroxide. This analysis implies that while  $\text{CaCrO}_3$  has an inherent tendency to produce  $\text{O}^*$  species, the formation of hydrogen peroxide is expected with a free energy difference of 0.1 eV.

Hydrogen peroxide ( $\text{H}_2\text{O}_2$ ) formation is particularly pronounced on the  $\text{CaMnO}_3$  and  $\text{CaFeO}_3$  surfaces. In the initial oxidation step, hydroxyl species are adsorbed with lower

energetic requirements compared to the direct formation of hydroxyl radicals. Subsequently, the system exhibits thermodynamic feasibility, supporting a pathway conducive to  $\text{H}_2\text{O}_2$  generation.

For the late transition metal oxides,  $\text{CaCoO}_3$  and  $\text{CaNiO}_3$ , the free energy required for the initial oxidation step exceeds that of the solvated hydroxyl radical ( $\Delta G_{\text{OH}(aq)} = 2.4$  eV) by 0.2 and 0.1 eV, respectively. This suggests that, upon formation of surface-bound  $\text{OH}^*$ , there is a thermodynamic preference for the species to either desorb as a solvated hydroxyl radical or recombine on the surface to form a hydroxyl group. In the second oxidation step of water oxidation,  $\text{CaCoO}_3$  exhibits comparable energetics for the formation of both metal-oxo species and hydrogen peroxide, leading to the coexistence of these products. In contrast,  $\text{CaNiO}_3$  stabilizes the metal-oxo intermediate with an energetic preference of approximately 0.2 eV, favoring the pathway toward the oxygen evolution reaction over hydrogen peroxide formation.

**Activity Trends.** A systematic decrease in the Gibbs free energy of hydrogen peroxide has been observed across the perovskite series from  $\text{CaTiO}_3$  to  $\text{CaFeO}_3$  (Figure 3a). In the case of late transition metals such as cobalt (Co) and nickel (Ni), the Gibbs free energy increases as the polaronic effect diminishes. Notably, iron (Fe) with an  $e_g^1$  occupancy exhibits a Jahn–Teller polaron and the lowest Gibbs free energy for this reaction. This demonstrates that the polaronic effect is the initiating factor in the evolution of hydrogen peroxide.

The free energy levels of various reaction intermediates, including  $\text{OH}^*$  (Figure 3b),  $\text{O}^*$  (Figure 3c), and  $\text{OOH}^*$

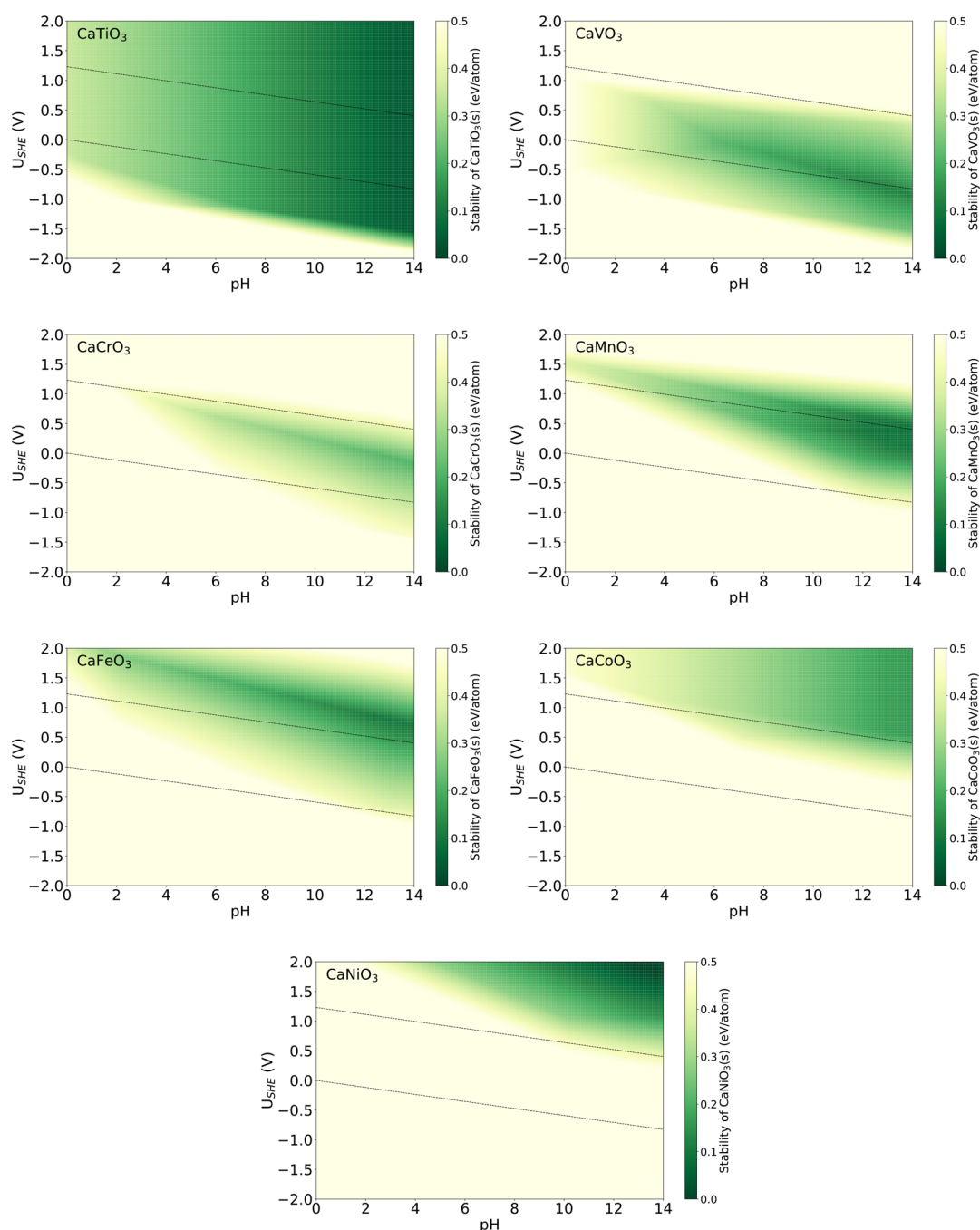


**Figure 5.** Bulk stability region of  $\text{CaMO}_3$  under a concentration of  $10^{-8}$  mol/L aqueous species. Pourbaix diagrams illustrating the most stable aqueous phases of  $\text{CaMO}_3$ . The green-shaded region represents the stable bulk phase, where the formation of  $\text{CaMO}_3$  from the solvated ions occurs spontaneously. The black dashed lines indicate the equilibrium boundaries for  $\text{O}_2/\text{H}_2\text{O}$  (upper line) and  $\text{H}_2/\text{H}_2\text{O}$  (lower line).

(Figure 3d), exhibit a correlation in energy. Specifically,  $\text{OH}^*$  displays a trend analogous to that of hydrogen peroxide, while both  $\text{O}^*$  and  $\text{OOH}^*$  demonstrate similar behavior with the exception of vanadium(V). It is important to note that this comparison is intended to be qualitative in nature, as  $\text{OH}^*$  corresponds to the initial proton–electron transfer step, while  $\text{H}_2\text{O}_2$  and  $\text{O}^*$  are produced in the subsequent proton–electron transfer and therefore occupy a higher free energy level. These analogous trends establish a linear scaling relation between intermediate binding energies, which is well-documented for catalytic surfaces of metals and metal oxides.<sup>9,48,49</sup> Notably,

linear correlations such as those observed between  $\text{OH}^*$  and  $\text{O}^*$  binding energies (where a slope of approximately 0.5 indicates the bonding difference) exemplify these scaling relationships:  $\text{O}^*$ , with dual surface bonds, exhibits stronger binding compared to  $\text{OH}^*$ , which forms a single bond to the surface.

The free energy difference between the values of the two aqueous groups of  $\text{O}^*$  and  $\text{OOH}^*$  exhibits minimal variation for  $3d$  orbital occupancy exceeding  $3d^2$ . This observation indicates that the polaronic effects on these two intermediates are negligible, suggesting that they do not significantly alter the binding strength.

In order to elucidate the influence of polarons on intermediate reactions, an investigation was conducted into the orbital representations of various bond characteristics in the studied systems. In the case of hydrogen peroxide (Figure 4a), hole localization occurs between two oxygen ions, facilitating the oxidation of water during the electrochemical process and ultimately yielding  $\text{H}_2\text{O}_2$ . A strong  $\sigma$  bond is formed between the two water molecules, which indicates the formation of an O–O bond. In this scenario, the strength of the metal–oxygen bond decreases, and hydrogen peroxide tends to desorb from the surface, indicating a tendency for release.

In contrast, the formation of a competing metal-oxo intermediate forms two different highly directional bonds with transition metals, depending upon the occupation of the  $3d$  orbitals. Upon interaction of the  $t_{2g}$  orbitals with oxygen (Figure 4b), the formation of a  $\pi$  bond is observed, indicating that neither a strong nor a weak bond is established. However, when the  $e_g$  orbitals interact with oxygen, a robust  $\sigma$  bond is formed, incorporating absorbed oxygen into the polarons of the compound (Figure 4c). This interaction demonstrates that the evolution of hydrogen peroxide occurs prior to the formation of metal-oxo intermediates. These findings suggest that the stabilization arising from polaron formation noticeably increases the surface ability to localize holes in an aqueous environment. A recent study,<sup>50</sup> consistent with our findings, presents the successful fabrication of highly efficient two-electron water oxidation electrocatalysts, particularly for Mn and Co perovskite oxide, which exhibits exceptional hydrogen peroxide production rates and outstanding stability over a 120-h test. By selecting optimal transition metals, incorporating polarons, and enhancing the adsorption characteristics of  $\text{O}^*$  and  $\text{OH}^*$ , an effective approach can be devised for the design of perovskite catalysts that are capable of efficient two- and four-electron water oxidation.

**pH-Dependent Thermodynamic Stability.** Although the polaronic competition in perovskites determines the OER activity, the bulk stability region of  $\text{CaMO}_3$  in an aqueous environment is still elusive. To explore the pH-dependent stability of  $\text{CaMO}_3$  perovskites, we have calculated the Pourbaix diagrams with respect to their ground-state perovskite structures, as shown in Figure 5. All graphs represent the equilibrium conditions of  $\text{CaMO}_3$  with the concentration of charged solvated ions  $10^{-8}$  mol/L. The area filled by the green color is the stable bulk region, in which the formation of  $\text{CaMO}_3$  from the solvated ions is spontaneous. We found that the stabilities significantly depend on both the pH and potential in an aqueous environment. None of the compounds is stable in an aqueous environment at  $\text{pH} = 0$ , while the formation of perovskite oxides is pronounced in an aqueous environment at a high pH value of 14. The stability region of  $\text{CaTiO}_3$  perovskite and aqueous ions was found to be in a broad range of the electrode potential and pH environments. However, the phase stability of other  $3d$  metals is more evident at  $\text{pH} = 14$  and at a portion of the potential, which shifts by adding electrons in the  $3d$  orbitals.

$\text{CaVO}_3$  demonstrated stability at lower potentials relative to the redox potential of the  $\text{O}_2/\text{H}_2\text{O}$ , with stability across a pH range exceeding 6. At higher pH, the stability of  $\text{CaVO}_3$  broadens toward potentials below the redox potential of the  $\text{H}_2/\text{H}_2\text{O}$ .  $\text{CaCrO}_3$  exhibited a more limited stability range, predominantly confined between the  $\text{O}_2/\text{H}_2\text{O}$  and  $\text{H}_2/\text{H}_2\text{O}$  redox potential lines at pH values above 6, although it did not maintain stability as effectively as  $\text{CaVO}_3$ . In contrast,  $\text{CaMnO}_3$

demonstrated stability closer to the redox potential of the  $\text{O}_2/\text{H}_2\text{O}$  across a broad pH range (3–14), with its stability region extending to lower potentials relative to the redox potential of the  $\text{H}_2/\text{H}_2\text{O}$  at higher pH levels. The stability region of  $\text{CaFeO}_3$  exhibits a notable upward shift in potential compared to that of its analogue,  $\text{CaMnO}_3$ , positioning it above the  $\text{O}_2/\text{H}_2\text{O}$  redox potential line. Late transition metal perovskites,  $\text{CaCoO}_3$  and  $\text{CaNiO}_3$ , displayed improved stability at potentials above the  $\text{O}_2/\text{H}_2\text{O}$  threshold.

The findings align with those of a prior experimental study<sup>51</sup> conducted under conditions where  $U_{\text{RHE}}$  was maintained at 1.6 V and the pH was set to 13. The results of these studies demonstrate that the concentration of aqueous species approaches approximately  $10^{-8}$  M. Therefore, we propose that elevated pH levels, along with the precise regulation of potentials in aqueous environments, significantly enhance catalytic activity for the OER and the production of hydrogen peroxide.

## SUMMARY

This study examines the fundamental processes that shed light on the water oxidation mechanisms in a series of calcium perovskite oxides,  $\text{CaMO}_3$ . To elucidate competing reaction pathways, periodic DFT calculations are employed. In particular, we examine the competition between the two proton–electron transfer pathways for the production of hydrogen peroxide and the four proton–electron transfer pathways for the OER. In the case of early transition metal (M) perovskites, oxygen species display  $\pi$ -bonding characteristics at the surface, which align with the conventional metal-oxo intermediate-driven OER mechanism. However, Mn- and Fe-based perovskites have been observed to strengthen surface-adsorbed oxygen species, promoting hole localization between adjacent oxygen atoms instead of direct proton transfer. This results in a preference for hydrogen peroxide production over OER.

Late transition metals, such as cobalt (Co), display dual functionality, participating in both oxygen evolution and hydrogen peroxide production. This is due to the existence of closely matched free energy profiles for each of these pathways. It is noteworthy that Ni displays a pronounced tendency toward oxygen evolution, exhibiting a clear preference for the OER pathway. A molecular orbital analysis indicates that hole localization, which is associated with polaronic effects, enhances the evolution of hydrogen peroxide by creation of the strong  $\sigma$  bond for the metal-oxo intermediate. These polaronic effects lead to a shift in selectivity and strengthen the metal-oxo bonding; thus, they enable a transition from conventional OER to  $\text{H}_2\text{O}_2$  evolution. It has been observed that hole localization frequently occurs between hydroxide and water molecules, which results in the disruption of hydrogen bonding and the formation of a distinctive hemibonded structure on the oxide surface.

Furthermore, our findings investigate the pH-dependent stability of perovskite structures, indicating that Ti-based perovskites exhibit robust stability across a range of pH values and electrochemical potentials. In contrast, other transition metals display stability predominantly at high pH ( $\text{pH} = 14$ ), and late transition metals show enhanced stability at elevated potentials. This study provides new insights into the mechanistic pathways and structural stability factors influencing water oxidation in calcium perovskites, with implications for optimizing the catalytic efficiency in water-splitting applications.



## METHODS

**Computational Details.** First-principles calculations are performed in the framework of density-functional theory (DFT)<sup>52,53</sup> on ternary  $\text{CaMO}_3$  perovskite compounds. The exchange-correlation effects were described by the generalized gradient approximation (GGA) functional RPBE<sup>54</sup> employing the projector augmented wave (PAW)<sup>55</sup> method as implemented in the Vienna Ab-initio Simulation Package.<sup>56–58</sup>

A plane wave cutoff of 520 eV was chosen for the wave functions, which was verified to provide converged total energies for all systems studied and a convergence within  $1 \times 10^{-5}$  eV per supercell. The *p* and *s* semicore states are treated as valence states for the transition metals and Ca, respectively. To properly describe the strongly correlated 3*d*-electrons, the Hubbard *U* corrections<sup>59</sup> on the transition metal 3*d* orbitals are set to  $U_V = 3.25$  eV,  $U_{Cr} = 3.70$  eV,  $U_{Mn} = 3.90$  eV,  $U_{Fe} = 5.30$  eV,  $U_{Co} = 3.32$  eV, and  $U_{Ni} = 6.20$  eV.<sup>60</sup> For Ti, only the conventional GGA-RPBE functional is used without the *U* parameter, as  $\text{Ti}^{4+}$  has an empty 3*d* shell and thus does not require a Hubbard correction. A  $4 \times 4 \times 3$  k-point mesh has been used for the unit cell of  $\text{CaMO}_3$ , containing four formula units, while the slab calculations were performed using a gamma-centered k-point grid. The initial configurations are taken from the Materials Project (MP) database.<sup>60</sup> We used the *Pnma* space group for  $\text{CaMO}_3$  perovskites, crystallizing in a face-centered cubic structure. All atomic positions are optimized without symmetry constraints to reach the theoretical ground state configurations. To correctly describe van der Waals interactions resulting from dynamical correlations between fluctuating charge distributions, the DFT-D3<sup>61</sup> method with Becke-Jonson damping has been applied in all the calculations. The RPBE+U+D3 approach used in this work has been extensively validated for transition metal oxides, and the calculated adsorption and reaction energetics are consistent with reported values,<sup>11</sup> thus confirming the reliability of the computational setup.

For periodic slab calculations, slabs of five layers in the (001) direction are separated by at least 26 Å of vacuum to prevent interactions due to periodic boundary conditions. Along the (001) direction,  $\text{CaMO}_3$  consists of alternating CaO and  $\text{MO}_2$  layers, resulting in both polar and nonpolar slab terminations. However, polar terminations introduce internal electric fields that are energetically unfavorable and are usually compensated for under realistic catalytic conditions. Therefore, we consider the optimized supercell of nonpolar slabs with  $\text{MO}_2$ -terminated surfaces. Each slab comprises eight transition metal atoms in the surface plane with lateral supercell dimensions greater than 10 Å. To keep the symmetry and cancel the artificial interaction between the system and its periodic images, on the top and bottom of the slabs, we have equivalent surfaces, both covered by 32 water molecules. The initial configuration was constructed using an ice-like hydrogen-bonded network to ensure full connectivity among water molecules. A full geometry optimization of both the surface and water molecules was performed to relax the interface. Despite the absence of configurational sampling (e.g., AIMD or ensemble averaging) due to computational constraints, the same optimized water structure was consistently applied across all surfaces. This approach provides a physically motivated and uniform solvation environment that captures key hydrogen-bonding effects while enabling a reliable comparison of trends between different materials. All atomic positions of the slabs are allowed to relax. Spin polarization is considered in all the calculations.

Proton-coupled electron transfer steps were modeled by sequentially deprotonating adsorbed water molecules, simulating the formation of  $\text{OH}^*$ ,  $\text{O}^*$ , and  $\text{OOH}^*$  species. Each deprotonation corresponds to the removal of one  $\text{H}^+ + \text{e}^-$  pair, mimicking surface oxidation (i.e., hole injection) while maintaining overall charge neutrality. This method is consistent with the established practice for simulating redox processes on oxide surfaces within periodic DFT. In order to ensure consistency, all adsorption energies were referenced to the clean solvated slab, taking into account the explicit water solvation.

**OER Free Energy Calculations.** To compute the free energy of reaction intermediates, we applied the computational hydrogen electrode (CHE) model as described by Nørskov et al.<sup>8</sup> This model enables the calculation of reaction free energies by incorporating the zero-point energy difference  $\Delta\text{ZPE}$ , the entropy change  $TS^0$ , and the effect of an applied potential  $eU$ . These factors are considered through the following equations:

$$\Delta G_{\text{OH}^*} = E_{\text{DFT}}^{\text{OH}^*} - E_{\text{DFT}}^{\text{H}_2\text{O}^*} + \frac{1}{2}E_{\text{DFT}}^{\text{H}_2(\text{g})} + (\Delta\text{ZPE} - TS^0) + k_{\text{B}}T \ln a_{\text{H}} - eU \quad (1)$$

$$\Delta G_{\text{O}^*} = E_{\text{DFT}}^{\text{O}^*} - E_{\text{DFT}}^{\text{OH}^*} + \frac{1}{2}E_{\text{DFT}}^{\text{H}_2(\text{g})} + (\Delta\text{ZPE} - TS^0) + k_{\text{B}}T \ln a_{\text{H}} - eU \quad (2)$$

$$\Delta G_{\text{H}_2\text{O}_2} = E_{\text{DFT}}^{\text{H}_2\text{O}_2} - E_{\text{DFT}}^{\text{OH}^*} + \frac{1}{2}E_{\text{DFT}}^{\text{H}_2(\text{g})} + (\Delta\text{ZPE} - TS^0) + k_{\text{B}}T \ln a_{\text{H}} - eU \quad (3)$$

$$\Delta G_{\text{OOH}^*} = E_{\text{DFT}}^{\text{OOH}^*} - E_{\text{DFT}}^{\text{O}^*} + \frac{1}{2}E_{\text{DFT}}^{\text{H}_2(\text{g})} + (\Delta\text{ZPE} - TS^0) + k_{\text{B}}T \ln a_{\text{H}} - eU \quad (4)$$

$$\Delta G_{\text{O}_2^*} = E_{\text{DFT}}^{\text{O}_2^*} - E_{\text{DFT}}^{\text{OOH}^*} + \frac{1}{2}E_{\text{DFT}}^{\text{H}_2(\text{g})} + (\Delta\text{ZPE} - TS^0) + k_{\text{B}}T \ln a_{\text{H}} - eU \quad (5)$$

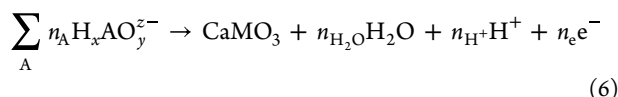
where  $E_{\text{DFT}}$  denotes the density functional theory (DFT)-calculated electronic energy for each specific intermediate. Here,  $E_{\text{DFT}}^{\text{H}_2(\text{g})}$  is the computed total electronic energy for the gaseous hydrogen molecule used as a reference. For computational efficiency, temperature contributions to enthalpy are approximated as negligible between 0 and 298 K. These calculations assume an associative mechanism for  $\text{O}_2$  formation on the catalyst. This approach only accounts for the elementary reaction steps, and no barriers are included. This means that the method presented here is necessary but not sufficient.

All corrections relative to the DFT total energy are summarized in Table 1

**Table 1. Room Temperature Corrections for the Zero-Point Energy and Entropy of Various Species**

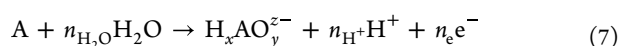
species	(ZPE-TS)/eV
$\text{H}_2\text{O}(\text{g})$	0.10
$\text{H}_2(\text{g})$	−0.13
$\text{O}^*$ adsorbate	0.01
$\text{OH}^*$ adsorbate	0.23
$\text{OOH}^*$ adsorbate	0.15

**Evaluating the Bulk Stability Region.** The methodology employed to determine the bulk stability region is based on describing the pH-*U* stability domain, where the following electrochemical reaction is thermodynamically favorable:



In this equation, the summation encompasses all elements denoted as “A” within the bulk material, with  $n_A$ ,  $n_{\text{H}_2\text{O}}$ ,  $n_{\text{H}^+}$ , and  $n_{\text{e}^-}$  representing the stoichiometric coefficients for elements A, water ( $\text{H}_2\text{O}$ ), protons ( $\text{H}^+$ ), and electrons ( $\text{e}^-$ ), respectively.

The species  $\text{H}_x\text{AO}_y^{z-}$  is defined as the most thermodynamically stable aqueous species of element “A” at specified pH and electrochemical potential (*U*). The specific form of  $\text{H}_x\text{AO}_y^{z-}$  is identified by selecting the species with the lowest formation energy, as indicated by the following reaction:



By precisely characterizing the bulk stability region of  $\text{CaMO}_3$ , we can establish a foundational understanding of the mechanisms driving the OER and the influence of various aqueous ions on this process. A comparable methodology has been previously utilized in the literature.<sup>62,63</sup>

The construction of Pourbaix diagrams was facilitated by the Materials Project (MP) methodology developed by Persson,<sup>64,65</sup> utilizing the Pymatgen software framework.<sup>66</sup> The stable regions within the Pourbaix diagrams are established based on potential equilibrium redox reactions relevant to the chemical composition under investigation.

## ■ ASSOCIATED CONTENT

### Data Availability Statement

All data are freely available at <https://doi.org/10.5281/zenodo.15696277>.

## ■ AUTHOR INFORMATION

### Corresponding Authors

**Mohsen Sotoudeh** – Institute of Theoretical Chemistry, Ulm University, 89081 Ulm, Germany; Helmholtz Institute Ulm (HIU) for Electrochemical Energy Storage, 89081 Ulm, Germany; Karlsruhe Institute of Technology (KIT), D-76021 Karlsruhe, Germany; [orcid.org/0000-0002-0970-5336](https://orcid.org/0000-0002-0970-5336); Email: [mohsen.sotoudeh@kit.edu](mailto:mohsen.sotoudeh@kit.edu)

**Axel Groß** – Institute of Theoretical Chemistry, Ulm University, 89081 Ulm, Germany; Helmholtz Institute Ulm (HIU) for Electrochemical Energy Storage, 89081 Ulm, Germany; [orcid.org/0000-0003-4037-7331](https://orcid.org/0000-0003-4037-7331); Email: [axel.gross@uni-ulm.de](mailto:axel.gross@uni-ulm.de)

Complete contact information is available at: <https://pubs.acs.org/10.1021/acscatal.5c02069>

### Notes

The authors declare no competing financial interest.

## ■ ACKNOWLEDGMENTS

This work contributes to the research performed at CELEST (Center for Electrochemical Energy Storage Ulm-Karlsruhe) and was funded by the German Research Foundation (DFG) under Project ID 390874152 (POLiS Cluster of Excellence). Computer time provided by the state of Baden-Württemberg through bwHPC and the German Research Foundation (DFG)

through grant no INST 40/575-1 FUGG (JUSTUS 2 cluster) is gratefully acknowledged.

## ■ REFERENCES

- (1) Gray, H. B. Powering the planet with solar fuel. *Nat. Chem.* **2009**, *1*, 7–7.
- (2) Castelli, I. E.; Landis, D. D.; Thygesen, K. S.; Dahl, S.; Chorkendorff, I.; Jaramillo, T. F.; Jacobsen, K. W. New cubic perovskites for one- and two-photon water splitting using the computational materials repository. *Energy Environ. Sci.* **2012**, *5*, 9034–9043.
- (3) Desmond Ng, J. W.; Gorlin, Y.; Hatsukade, T.; Jaramillo, T. F. A Precious-Metal-Free Regenerative Fuel Cell for Storing Renewable Electricity. *Adv. Energy Mater.* **2013**, *3*, 1545–1550.
- (4) Cao, R.; Lee, J.-S.; Liu, M.; Cho, J. Recent Progress in Non-Precious Catalysts for Metal-Air Batteries. *Adv. Energy Mater.* **2012**, *2*, 816–829.
- (5) Juárez, F.; Yin, H.; Groß, A. Composition and Electronic Structure of  $\text{Mn}_3\text{O}_4$  and  $\text{Co}_3\text{O}_4$  Cathodes in Zinc–Air Batteries: A DFT Study. *J. Phys. Chem. C* **2022**, *126*, 2561–2572.
- (6) Sathiyar, M.; Rousse, G.; Ramesha, K.; Laisa, C. P.; Vezin, H.; Sougrati, M. T.; Doublet, M.-L.; Foix, D.; Gonbeau, D.; Walker, W.; Prakash, A. S.; Ben Hassine, M.; Dupont, L.; Tarascon, J.-M. Reversible anionic redox chemistry in high-capacity layered-oxide electrodes. *Nat. Mater.* **2013**, *12*, 827–835.
- (7) Zhang, M.; Kitchaev, D. A.; Lebens-Higgins, Z.; Vinckeviciute, J.; Zuba, M.; Reeves, P. J.; Grey, C. P.; Whittingham, M. S.; Piper, L. F. J.; Van der Ven, A.; Meng, Y. S. Pushing the limit of 3d transition metal-based layered oxides that use both cation and anion redox for energy storage. *Nat. Rev. Mater.* **2022**, *7*, 522–540.
- (8) Nørskov, J. K.; Rossmeisl, J.; Logadottir, A.; Lindqvist, L.; Kitchin, J. R.; Bligaard, T.; Jónsson, H. Origin of the Overpotential for Oxygen Reduction at a Fuel-Cell Cathode. *J. Phys. Chem. B* **2004**, *108*, 17886–17892.
- (9) Rossmeisl, J.; Qu, Z.-W.; Zhu, H.; Kroes, G.-J.; Nørskov, J. Electrolysis of water on oxide surfaces. *J. Electroanal. Chem.* **2007**, *607*, 83–89.
- (10) Koper, M. T. M. Theory of multiple proton–electron transfer reactions and its implications for electrocatalysis. *Chem. Sci.* **2013**, *4*, 2710–2723.
- (11) Man, I. C.; Su, H.-Y.; Calle-Vallejo, F.; Hansen, H. A.; Martínez, J. I.; Inoglu, N. G.; Kitchin, J.; Jaramillo, T. F.; Nørskov, J. K.; Rossmeisl, J. Universality in Oxygen Evolution Electrocatalysis on Oxide Surfaces. *ChemCatChem* **2011**, *3*, 1159–1165.
- (12) Suntivich, J.; May, K. J.; Gasteiger, H. A.; Goodenough, J. B.; Shao-Horn, Y. A Perovskite Oxide Optimized for Oxygen Evolution Catalysis from Molecular Orbital Principles. *Science* **2011**, *334*, 1383–1385.
- (13) Grimaud, A.; Hong, W. T.; Shao-Horn, Y.; Tarascon, J. M. Anionic redox processes for electrochemical devices. *Nat. Mater.* **2016**, *15*, 121–126.
- (14) Grimaud, A.; Diaz-Morales, O.; Han, B.; Hong, W. T.; Lee, Y.-L.; Giordano, L.; Stoerzinger, K. A.; Koper, M. T. M.; Shao-Horn, Y. Activating lattice oxygen redox reactions in metal oxides to catalyze oxygen evolution. *Nat. Chem.* **2017**, *9*, 457–465.
- (15) Mefford, J. T.; Rong, X.; Abakumov, A. M.; Hardin, W. G.; Dai, S.; Kolpak, A. M.; Johnston, K. P.; Stevenson, K. J. Water electrolysis on  $\text{La}_{1-x}\text{Sr}_x\text{CoO}_{3-\delta}$  perovskite electrocatalysts. *Nat. Commun.* **2016**, *7*, 11053.
- (16) Matsumoto, Y.; Manabe, H.; Sato, E. Oxygen Evolution on  $\text{La}_{1-x}\text{Sr}_x\text{CoO}_3$  Electrodes in Alkaline Solutions. *J. Electrochem. Soc.* **1980**, *127*, 811.
- (17) Giordano, L.; Han, B.; Risch, M.; Hong, W. T.; Rao, R. R.; Stoerzinger, K. A.; Shao-Horn, Y. pH dependence of OER activity of oxides: Current and future perspectives. *Catal. Today* **2016**, *262*, 2–10.
- (18) Huang, J.; Li, M.; Eslamibidgoli, M. J.; Eikerling, M.; Groß, A. Cation Overcrowding Effect on the Oxygen Evolution Reaction. *JACS Au* **2021**, *1*, 1752–1765.



- (19) Shi, X.; Siahrostami, S.; Li, G.-L.; Zhang, Y.; Chakthranont, P.; Studt, F.; Jaramillo, T. F.; Zheng, X.; Nørskov, J. K. Understanding activity trends in electrochemical water oxidation to form hydrogen peroxide. *Nat. Commun.* **2017**, *8*, 701.
- (20) Mavrikis, S.; Göltz, M.; Perry, S. C.; Bogdan, F.; Leung, P. K.; Rosiwal, S.; Wang, L.; Ponce de León, C. Effective Hydrogen Peroxide Production from Electrochemical Water Oxidation. *ACS Energy Lett.* **2021**, *6*, 2369–2377.
- (21) Brillas, E.; Sirés, I.; Oturan, M. A. Electro-Fenton Process and Related Electrochemical Technologies Based on Fenton's Reaction Chemistry. *Chem. Rev.* **2009**, *109*, 6570–6631.
- (22) Fukuzumi, S.; Yamada, Y.; Karlin, K. D. Hydrogen peroxide as a sustainable energy carrier: Electrocatalytic production of hydrogen peroxide and the fuel cell. *Electrochim. Acta* **2012**, *82*, 493–511.
- (23) Siahrostami, S. Rechargeable Metal–Hydrogen Peroxide Battery, A Solution to Improve the Metal–Air Battery Performance. *ACS Energy Lett.* **2022**, *7*, 2717–2724.
- (24) Siahrostami, S.; Li, G.-L.; Viswanathan, V.; Nørskov, J. K. One- or Two-Electron Water Oxidation, Hydroxyl Radical, or H<sub>2</sub>O<sub>2</sub> Evolution. *J. Phys. Chem. Lett.* **2017**, *8*, 1157–1160.
- (25) Woodward, P. M. Tilting Octahedral in Perovskites. II. Structure Stabilizing Forces. *Acta Crystallogr. B* **1997**, *53*, 44–66.
- (26) Sotoudeh, M.; Rajpurohit, S.; Blöchl, P.; Mierwaldt, D.; Norpoth, J.; Roddatis, V.; Mildner, S.; Kressdorf, B.; Iffland, B.; Jooss, C. Electronic structure of Pr<sub>1-x</sub>Ca<sub>x</sub>MnO<sub>3</sub>. *Phys. Rev. B* **2017**, *95*, No. 235150.
- (27) Sotoudeh, M.; Dillenz, M.; Groß, A. Mechanism of Magnesium Transport in Spinel Chalcogenides. *Adv. Energy Sustainability Res.* **2021**, *2*, No. 2100113.
- (28) Raiser, D.; Mildner, S.; Iffland, B.; Sotoudeh, M.; Blöchl, P.; Techert, S.; Jooss, C. Evolution of Hot Polaron States with a Nanosecond Lifetime in a Manganite Perovskite. *Adv. Energy Mater.* **2017**, *7*, No. 1602174.
- (29) Franchini, C.; Reticcioli, M.; Setvin, M.; Diebold, U. Polarons in materials. *Nat. Rev. Mater.* **2021**, *6*, 560–586.
- (30) Sotoudeh, M.; Bongers-Loth, M. D.; Roddatis, V.; Čížek, J.; Nowak, C.; Wenderoth, M.; Blöchl, P.; Pundt, A. Hydrogen-related defects in titanium dioxide at the interface to palladium. *Phys. Rev. Mater.* **2021**, *5*, No. 125801.
- (31) Daoud-Aladine, A.; Rodríguez-Carvajal, J.; Pinsard-Gaudart, L.; Fernández-Díaz, M. T.; Revcolevschi, A. Zener Polaron Ordering in Half-Doped Manganites. *Phys. Rev. Lett.* **2002**, *89*, No. 097205.
- (32) Ren, Z.; Shi, Z.; Feng, H.; Xu, Z.; Hao, W. Recent Progresses of Polarons: Fundamentals and Roles in Photocatalysis and Photoelectrocatalysis. *Adv. Sci.* **2024**, *11*, No. 2305139.
- (33) Setvin, M.; Franchini, C.; Hao, X.; Schmid, M.; Janotti, A.; Kaltak, M.; Van de Walle, C. G.; Kresse, G.; Diebold, U. Direct View at Excess Electrons in TiO<sub>2</sub> Rutile and Anatase. *Phys. Rev. Lett.* **2014**, *113*, No. 086402.
- (34) Yim, C. M.; Watkins, M. B.; Wolf, M. J.; Pang, C. L.; Hermansson, K.; Thornton, G. Engineering Polarons at a Metal Oxide Surface. *Phys. Rev. Lett.* **2016**, *117*, No. 116402.
- (35) Chen, C.; Avila, J.; Frantzeskakis, E.; Levy, A.; Asensio, M. C. Observation of a two-dimensional liquid of Fröhlich polarons at the bare SrTiO<sub>3</sub> surface. *Nat. Commun.* **2015**, *6*, 8585.
- (36) Carneiro, L. M.; Cushing, S. K.; Liu, C.; Su, Y.; Yang, P.; Alivisatos, A. P.; Leone, S. R. Excitation-wavelength-dependent small polaron trapping of photoexcited carriers in  $\alpha$ -Fe<sub>2</sub>O<sub>3</sub>. *Nat. Mater.* **2017**, *16*, 819–825.
- (37) Wu, H.; Zhang, L.; Qu, S.; Du, A.; Tang, J.; Ng, Y. H. Polaron-Mediated Transport in BiVO<sub>4</sub> Photoanodes for Solar Water Oxidation. *ACS Energy Lett.* **2023**, *8*, 2177–2184.
- (38) Reticcioli, M.; Setvin, M.; Hao, X.; Flaugar, P.; Kresse, G.; Schmid, M.; Diebold, U.; Franchini, C. Polaron-Driven Surface Reconstructions. *Phys. Rev. X* **2017**, *7*, No. 031053.
- (39) Reticcioli, M.; Sokolović, I.; Schmid, M.; Diebold, U.; Setvin, M.; Franchini, C. Interplay between Adsorbates and Polarons: CO on Rutile TiO<sub>2</sub>(110). *Phys. Rev. Lett.* **2019**, *122*, No. 016805.
- (40) Tanner, A. J.; Wen, B.; Zhang, Y.; Liu, L.-M.; Fielding, H. H.; Selloni, A.; Thornton, G. Photoexcitation of bulk polarons in rutile TiO<sub>2</sub>. *Phys. Rev. B* **2021**, *103*, No. L121402.
- (41) Gono, P.; Wiktor, J.; Ambrosio, F.; Pasquarello, A. Surface Polarons Reducing Overpotentials in the Oxygen Evolution Reaction. *ACS Catal.* **2018**, *8*, 5847–5851.
- (42) Wiktor, J.; Ambrosio, F.; Pasquarello, A. Role of Polarons in Water Splitting: The Case of BiVO<sub>4</sub>. *ACS Energy Lett.* **2018**, *3*, 1693–1697.
- (43) Busch, M.; Sotoudeh, M. The role of exact exchange on the structure of water dimer radical cation: Hydrogen bond vs hemibond. *J. Chem. Phys.* **2023**, *159*, No. 034303.
- (44) Chipman, D. M. Hemibonding between Water Cation and Water. *J. Phys. Chem. A* **2016**, *120*, 9618–9624.
- (45) Cheng, Q.; Evangelista, F. A.; Simmonett, A. C.; Yamaguchi, Y.; Schaefer, H. F. I. Water Dimer Radical Cation: Structures, Vibrational Frequencies, and Energetics. *J. Phys. Chem. A* **2009**, *113*, 13779–13789.
- (46) Groß, A. Reversible vs Standard Hydrogen Electrode Scale in Interfacial Electrochemistry from a Theoretician's Atomistic Point of View. *J. Phys. Chem. C* **2022**, *126*, 11439–11446.
- (47) Cuzzati, F. L.; Parras, G. A. S.; Freitas, G. D. S.; Parizi, M. P. S.; Souza, A. E. d. CaTiO<sub>3</sub>: Influence of Ag Doping on Photocatalytic Activity for Application in Rhodamine B dye Removal. *Mater. Res.* **2024**, *27*, No. e20240201.
- (48) Rossmel, J.; Logadottir, A.; Nørskov, J. Electrolysis of water on (oxidized) metal surfaces. *Chem. Phys.* **2005**, *319*, 178–184.
- (49) Abild-Pedersen, F.; Greeley, J.; Studt, F.; Rossmel, J.; Munter, T. R.; Moses, P. G.; Skúlason, E.; Bligaard, T.; Nørskov, J. K. Scaling Properties of Adsorption Energies for Hydrogen-Containing Molecules on Transition-Metal Surfaces. *Phys. Rev. Lett.* **2007**, *99*, No. 016105.
- (50) Shao, H.; Zhang, C.; Jiang, H.; Guan, J.; Guan, W.; Shi, Q.; Hu, J. “B” site-modulated perovskite oxide materials for efficient electrochemical water oxidation to hydrogen peroxide. *Appl. Catal. A: Gen.* **2024**, *670*, No. 119558.
- (51) Kim, J.; Yin, X.; Tsao, K.-C.; Fang, S.; Yang, H. Ca<sub>2</sub>Mn<sub>2</sub>O<sub>5</sub> as Oxygen-Deficient Perovskite Electrocatalyst for Oxygen Evolution Reaction. *J. Am. Chem. Soc.* **2014**, *136*, 14646–14649.
- (52) Hohenberg, P.; Kohn, W. Inhomogeneous Electron Gas. *Phys. Rev.* **1964**, *136*, B864–B871.
- (53) Kohn, W.; Sham, L. J. Self-Consistent Equations Including Exchange and Correlation Effects. *Phys. Rev.* **1965**, *140*, A1133–A1138.
- (54) Hammer, B.; Hansen, L. B.; Nørskov, J. K. Improved adsorption energetics within density-functional theory using revised Perdew-Burke-Ernzerhof functionals. *Phys. Rev. B* **1999**, *59*, 7413–7421.
- (55) Blöchl, P. E. Projector augmented-wave method. *Phys. Rev. B* **1994**, *50*, 17953–17979.
- (56) Kresse, G.; Hafner, J. Ab initio molecular dynamics for liquid metals. *Phys. Rev. B* **1993**, *47*, 558–561.
- (57) Kresse, G.; Furthmüller, J. Efficient iterative schemes for ab initio total-energy calculations using a plane-wave basis set. *Phys. Rev. B* **1996**, *54*, 11169–11186.
- (58) Kresse, G.; Joubert, D. From ultrasoft pseudopotentials to the projector augmented-wave method. *Phys. Rev. B* **1999**, *59*, 1758–1775.
- (59) Dudarev, S. L.; Botton, G. A.; Savrasov, S. Y.; Humphreys, C. J.; Sutton, A. P. Electron-energy-loss spectra and the structural stability of nickel oxide: An LSDA+U study. *Phys. Rev. B* **1998**, *57*, 1505–1509.
- (60) Jain, A.; Ong, S. P.; Hautier, G.; Chen, W.; Richards, W. D.; Dacek, S.; Cholia, S.; Gunter, D.; Skinner, D.; Ceder, G.; Persson, K. A. Commentary: The Materials Project: A materials genome approach to accelerating materials innovation. *APL Mater.* **2013**, *1*, No. 011002.
- (61) Grimme, S.; Antony, J.; Ehrlich, S.; Krieg, H. A consistent and accurate ab initio parametrization of density functional dispersion correction (DFT-D) for the 94 elements H–Pu. *J. Chem. Phys.* **2010**, *132*, 154104.
- (62) Rong, X.; Parolin, J.; Kolpak, A. M. A Fundamental Relationship between Reaction Mechanism and Stability in Metal Oxide Catalysts for Oxygen Evolution. *ACS Catal.* **2016**, *6*, 1153–1158.

(63) Qiu, T.; Tu, B.; Saldana-Greco, D.; Rappe, A. M. Ab Initio Simulation Explains the Enhancement of Catalytic Oxygen Evolution on  $\text{CaMnO}_3$ . *ACS Catal.* **2018**, *8*, 2218–2224.

(64) Persson, K. A.; Waldwick, B.; Lazic, P.; Ceder, G. Prediction of solid-aqueous equilibria: Scheme to combine first-principles calculations of solids with experimental aqueous states. *Phys. Rev. B* **2012**, *85*, No. 235438.

(65) Singh, A. K.; Zhou, L.; Shinde, A.; Suram, S. K.; Montoya, J. H.; Winston, D.; Gregoire, J. M.; Persson, K. A. Electrochemical Stability of Metastable Materials. *Chem. Mater.* **2017**, *29*, 10159–10167.

(66) Ong, S. P.; Richards, W. D.; Jain, A.; Hautier, G.; Kocher, M.; Cholia, S.; Gunter, D.; Chevrier, V. L.; Persson, K. A.; Ceder, G. Python Materials Genomics (pymatgen): A robust, open-source python library for materials analysis. *Comput. Mater. Sci.* **2013**, *68*, 314–319.



**CAS BIOFINDER DISCOVERY PLATFORM™**

**PRECISION DATA  
FOR FASTER  
DRUG  
DISCOVERY**

CAS BioFinder helps you identify  
targets, biomarkers, and pathways

**Unlock insights**

**CAS**  
A division of the  
American Chemical Society